Macromolecules

ARTICLE

pubs.acs.org/Macromolecules

Morphology, Chain Dynamics, and Domain Sizes in Highly Drawn Gel-Spun Ultrahigh Molecular Weight Polyethylene Fibers at the Final Stages of Drawing by SAXS, WAXS, and ^{1}H Solid-State NMR

V. M. Litvinov,*,† Jianjun Xu,*,† C. Melian,† D. E. Demco,*,‡ M. Möller,‡ and J. Simmelink§

†DSM Resolve, P.O. Box 18, 6160 MD Geleen, The Netherlands

‡DWI an der RWTH-Universität Aachen e.V., Pauwelsstrasse 8, D-52074 Aachen, Germany

§DSM Dyneema, Mauritslaan 49, 6129 EL Urmond, The Netherlands

Supporting Information

ABSTRACT: Morphology, phase composition, and molecular mobility for a series of semicommercial gel-spun UHMWPE fibers were studied using a combination of WAXS, SAXS, and ^{1}H solid-state NMR methods. The fibers show uncommon for this type of fibers decrease in the break load with increasing draw ratio, whereas their modulus and the tenacity reach very high ultimate values. The X-ray and NMR methods have provided complementary information about the fiber morphology and structural reorganizations occurring at the final stage of the fiber drawing. The results suggest that the fiber morphology can be described by a mixture of crystalline fibrils with long period of ~35−45 nm, as shown by SAXS, and large, so-called, chain-extended crystals. The presence of large crystals with embedded defects is shown by NMR. The drawing causes increase in the crystallinity from ~89 to ~96 wt % and in chain orientation, while the long period of fibrils and the break load of fibers surprisingly decrease. The decrease in the long period with the drawing could indicate a partial reorganization of the amorphous phase and/or some fragmentation of the fibrils, while the decrease in the break load could correspond to a decrease in number of load-bearing chains. A disorder of the crystals and a small increase in chain mobility in the constrained amorphous fraction is also observed with increasing the drawing. Approximately 1 wt % of the chain fragments in the amorphous fraction has a high molecular mobility. It is assumed that these chain fragments reside in nanovoids, the presence of which was shown previously by a ^{129}Xe NMR study on the same fibers. The role of α-crystalline relaxation in structural reorganizations during fiber drawing is also discussed.

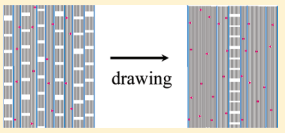

I. INTRODUCTION

Elucidating the structure of high-strength polymeric fibers is a very important issue in fiber technology research. Extensive work has been carried out in the past decades to find correlations between structure, performance, and processing conditions of fibers.[1,2] There are two types of super-strong polymeric fibers, mainly differentiated by the type of the chemical structure of polymer and the type of fiber processing. One type, such as Aramid and Zylon fibers, is based on relatively "stiff" polymer molecules. The other type is prepared from more flexible molecules, e.g. (ultra)high molecular weight polyethylene (UHMWPE). The performance of these polymeric fibers is the result of rather complex processing and deformation mechanisms due to drawing. A well-defined model was developed for Aramid fibers allowing the prediction of fiber performance purely based on the chemical structure and processing parameters.[2,3] For gel-spun UHMWPE fibers like Dyneema, such a model is not present, although significant effort has been placed into the research on the structure of this kind of fiber.[1,2]

Several methods have been developed for the production of high-modulus, high-strength structures based on UHMWPE, namely melt-spinning, gel-spinning, and solid-state drawing.[4] Both the tensile strength and the modulus of UHMWPE fibers increase with the drawing. To reach a higher draw ratio in the fiber, the UHMWPE polymer chains must have a low entanglement density to allow for polymer chain orientation during drawing. This effect can be realized by processing the UHMWPE material from a (semi)dilute solution where the polymer chains have been (partially) disentangled as part of the dissolution process. The strongest fibers are therefore produced using the gel-spinning method consisting of the following three main steps: (1) continuous extrusion of a dilute solution of UHMWPE, (2) spinning of the solution (followed by physical gelation of UHMWPE due to its fast crystallization caused by either cooling of the solution or solvent removal by extraction or evaporation), and (3) drawing of fibers at elevated temperatures.[5−7] The attainable draw ratio is affected by several factors such as molecular weight of the polymer, the drawing temperature, and the drawing speed.[8]

Drawing of gel-spun UHMWPE fibers results in changes in their physical structure. For example, at low draw ratio ($\lambda < 12$), crystallinity may decrease, whereas crystal orientation increases and approaches a high value already at a moderate draw ratio.[9,10] In contrast, chain orientation in the amorphous phase increases almost linearly with increasing draw ratio and approaches its maximum value at $\lambda \approx 100$.[10] The degree of crystallinity approaches its maximum value exceeding 90% at approximately

Received: August 18, 2011
Revised: October 20, 2011
Published: November 04, 2011

the same draw ratio.[10] In addition, the amount of monoclinic crystals grows gradually with an increasing draw ratio.

Different morphological elements are present in highly drawn UHMWPE gel-spun fibers,[11−14] and different types of morphological imperfections are found on the fiber surface.[12] However, fibrillar morphology is often the dominant one in highly drawn UHMWPE materials.[15] Fibrils are composed of submicrometer sized crystalline blocks that are interconnected by highly elongated chain fragments in amorphous and interfacial fractions. As proposed by several research groups, the phase structure of UHMWPE fibers consists of five components. Two are associated with the crystalline phase: (1) the majority of the crystalline phase is formed by orthorhombic crystals, and (2) a small amount of monoclinic phase is present in highly drawn fibers. The three other components are associated with the noncrystalline phase: (3) a crystal−amorphous interface that is adjacent to the crystal surface with chain units mainly in *all-trans* conformations, (4) amorphous regions that are formed by less ordered chain fragments in trans−gauche conformation, and (5) a small amount of highly mobile chain fragments in nanovoids.[16] The presence of nanovoids in highly drawn fibers was suggested by several studies.[17−20] It should be mentioned that such description of the phase composition is rather simplified because of the complexity of the fiber morphology, its heterogeneity, and the absence of sharp borders between the different phases.

Two types of models were proposed to explain the relationship between drawing-induced changes in physical structures and improvement of mechanical properties of UHMWPE fibers.[21] The morphology of gel-spun UHMWPE fibers at different draw ratios can be rather well described by a model that was proposed for drawn polyethylenes by Peterlin[22] and Gibson et al.[23] This *morphological model* assumes that the amount of taut-tie molecules that interconnect crystals plays an important role in the improvement of mechanical properties. An extended mechanism of morphological reorganizations during drawing was proposed more recently.[14,24] The increase of the modulus with increasing draw ratio correlates with the chain orientation in both crystalline and amorphous phases where the high chain orientation in the amorphous domains is necessary to achieve ultimate fiber strength.[10] The importance of taut-tie molecules for achieving high ultimate fiber properties was also suggested in another study.[25] Therefore, characterization of both crystalline and noncrystalline or "amorphous" phases in UHMWPE fibers is important for establishing processing−morphology−property relationships for highly drawn PE materials. In the *composite model approach*, the reinforcement is caused by oriented crystals that are embedded in a partially oriented amorphous phase.[26,27] Since both types of model, namely the morphological and composite model, can explain the effect of drawing on macroscopic properties of UHMWPE fibers,[14,27] a better understanding of how drawing effects the morphological changes is desired.

A variety of methods have been used for the characterization of the morphology and physical structures of UHMWPE fibers and tapes, such as microscopy methods, WAXS, SAXS, DSC, deformation calorimetry, solid-state NMR, and Raman spectroscopy as well as several other methods. Some of these studies are cited below, although this list of references is far from being complete. Morphology of highly drawn UHMWPE was studied by SAXS,[24,28−30] solid-state NMR,[16] and microscopy methods;[11,13−15] phase composition and dimensions of different phases by X-ray,[17,24,31−34] solid-state NMR,[16,20,35] and microscopy methods;[11,13−15] molecular mobility by solid-state NMR;[16,20,35] orientation by X-ray,[36−39] infrared dichroism,[10] and solid-state NMR;[35,40] the effect of deformation on chain loading by Raman spectroscopy and WAXS;[41] strain-induced chain scissions by ESR;[42] nanovoids by positron annihilation spectroscopy[19] and ^{129}Xe NMR;[20] and thermodynamics of small deformations of single crystal mats of PE by deformation calorimetry.[18]

Results of these different studies show that fiber properties largely depend on fiber technology and processing conditions. As mentioned earlier, the tensile modulus and the tensile strength of gel-spun UHMWPE fibers and drawn single crystal mats of UHMWPE rapidly increase with draw ratio and reach ultimate plateau values at draw ratios higher than ∼100−150 of ∼120−160 and ∼5−6 GPa, respectively.[9,10,13,43] Higher values for the ultimate properties (i.e., 220 and 6 GPa, respectively) were reported for drawn single crystal mats of UHMWPE,[44] indicating importance of the disentangled state of the polymer chains for obtaining the strongest UHMWPE fibers.

In the literature, several values for the maximum tensile strength and the modulus of UHMWPE fibers were estimated using theoretical calculations. These values, which are based on the strength of carbon−carbon bonds, are all in the range of 18−30 GPa for the tensile strength and ∼230−355 GPa for the modulus.[45−50] The experimental maximum tensile strength increases strongly with decreasing filament cross-section area due to the smaller number of surface flaws and kink bands per the length unit of fibers.[51] This increase can be explained by the Griffith theory[52,53] where for a cylindrical filament shape the Griffith relationship predicts a linear dependence of the reciprocal tensile strength on the square root of the filament diameter. Based on this theory and extrapolating this relationship to fiber diameter that approaches zero, a maximum theoretical tensile strength of 25 GPa was estimated. However, until present no experimental tensile strength higher than 8 GPa has been reported in the literature, while the maximum modulus values of up to 300 GPa were reported.[48] Thus, a significant gap still exists between the experimental tensile strength and its theoretical maximum value, whereas the experimental modulus of fibers are rather close to the theoretical value. This indicates that the tensile strength is not only affected by fiber structure, which tends to approach the single crystal at the maximum draw ratio, but also affected by local defects such as chain ends, defects in crystals, other fiber flaws, etc. It is therefore difficult to establish the relationship between the tensile strength and fiber morphology.

In order to improve ultimate properties of UHMWPE fibers, it is important to understand the structural and morphological changes at the final stage of the fiber drawing. For this purpose, we prepared a large series of samples with different draw ratios and, consequently, different mechanical properties that approach very high values at the highest draw ratio. Contrary to the most of previously studied series of UHMWPE fibers, fibers for the present study were spun from a (semi)dilute solution on a pilot production facility. The morphology, local chain motions, and domain sizes are characterized by a combination of SAXS, WAXS, and ^{1}H solid-state NMR. Although these methods have been extensively used for characterization of gel-spun UHMWPE fibers before, studies of a large series of fibers using a combination of these complementary methods have not been reported previously. The aim of the present study is to determine (1) the phase composition using WAXS and NMR relaxometry, (2) crystal dimensions by SAXS, WAXS, and ^{1}H NMR spin-diffusion methods (NMR has an advantage in estimation of the size of chain-extended crystals whose dimensions are beyond the

detection limit of conventional SAXS experiments), and (3) the effect of draw ratio on molecular mobility in different physical phases using NMR relaxometry and to discuss the effect of draw ratio on changes in morphology and the physical structures in relation to mechanical properties. This approach is very promising for gaining a better understanding the effect of draw ratio on morphology and mechanical properties of UHMWPE fibers.

II. EXPERIMENTAL SECTION

A. Fiber Preparation. All samples were produced at DSM Dyneema on a pilot production facility as 50 filament yarns using the well-described gel spinning process.[54] The feedstock was an UHMWPE with $M_w = 3.5 \times 10^6$ g/mol. UHMWPE fibers were spun from 9 wt % solution in decalin. Spin-finish was removed by washing fibers in *n*-pentane followed by drying in a flow of nitrogen gas.

The tensile strength and the tensile modulus were determined on the multifilament yarns as specified in ASTM D885M method using a nominal gauge fiber length of 500 mm, a crosshead speed of 50%/min, and Instron 2714 clamps. The modulus was determined from the stress−strain curve as the slope between 0.3 and 1.0% strain. The modulus and the tensile strength were calculated from the tensile force by dividing its value by the titer, which is mass of 10 m of yarn and assuming the volume average fiber density of 0.97 g/cm^3.

B. Wide-Angle X-ray Scattering. The 2D WAXS experiment were carried out on a D8 Discover goniometer from Bruker on a bundle of "pseudoparallel" filaments or a single filament placed vertically with the X-ray beam perpendicular to the fiber axis. The crystal size (d_c) was estimated using the Scherrer equation.[36−39] The amounts of the amorphous, monoclinic, and orthorhombic phases were calculated using eqs 1 and 2:

$$W_{c,o} = (A_{110} + 1.42A_{200})/(0.73A_{001}{}' + 1.25A_{200}{}' + 1.69A_{20-1}{}' + A_{110} + 1.42A_{200} + 0.65A_a) \quad (1)$$

$$W_{c,m} = (0.73A_{001}{}' + 1.25A_{200}{}' + 1.69A_{20-1}{}')/(0.73A_{001}{}' + 1.25A_{200}{}' + 1.69A_{20-1}{}' + A_{110} + 1.42A_{200} + 0.65A_a) \quad (2)$$

where A_a is the peak area of the amorphous phase, A_{110} and A_{200} are areas of the (110) and (200) peaks for the orthorhombic phase, and $A_{001}{}'$, $A_{200}{}'$, and $A_{20-1}{}'$ are areas for corresponding peaks of the monoclinic phase. The peak deconvolution was performed with the constraint conditions as described in the Supporting Information. These constraint conditions were necessary for obtaining reliable peak deconvolution for highly crystalline PE. To our knowledge, these constraint conditions were applied for the first time in the literature for the PE. The multiplication factors for each peak area were calculated in reference to the intensity of (110) peak of the orthorhombic phase with corrections considering geometry, polarization, temperature (thermal motion), and absorption.[36,38] The factor of 0.65 for A_a was used to compensate the diffraction peaks at 2θ larger than 28°.[38] More details of the calculations can be found in the Supporting Information.

The chain orientation was estimated using the full width at half-maximum (FWHM) of azimuthal intensity distribution of the (110) diffraction peak ($FWHM_{110}$).[55,56] For the experiment, a single filament of ∼12 cm length was measured at 10−12 different positions along the fiber axis, and the average value of $FWHM_{110}$ is reported. The Herman's orientation parameter $\langle P_2 \rangle$ was calculated from $FWHM_{110}$[39] using the relation $\langle P_2 \rangle_{002} = -2\langle P_2 \rangle_{110}$[57] and assuming a cylindrical symmetry with respect to the *c*-axis (chain direction).

C. Small-Angle X-ray Scattering. Two-dimensional (2D) SAXS experiments were carried out on a Point-Focusing SAXS System from Molecular Metrology,[58] using an Ar-based multiwire 2D detector.

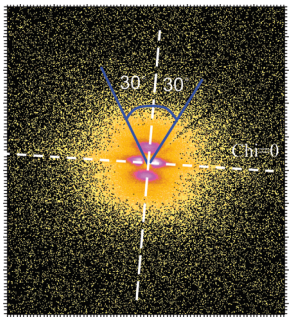

Figure 1. 2D SAXS pattern for a gel-spun UHMWPE fiber with a modulus of 28 GPa. One integration range in direction along the fiber axes is shown on the pattern.

The fibers were measured as a bundle of "pseudoparallel" filaments with the fiber axes placed vertical and the beam perpendicular to the filaments. The anisotropic 2D pattern was calibrated using silver behenate (d_{001}= 58.380 Å) and integrated in the ranges from 30° below to 30° above φ_{max} (fiber direction) on two opposite directions using Fit2D program from ESRF,[59] as shown in Figure 1. The scattering intensity (I) was plotted in the form of Iq^2 vs q (Lorentz-corrected form),[60] where q is the scattering vector which is determined from the following relationship $q = (4\pi/) \cdot \sin\theta$, where 2θ is the scattering angle. By applying Bragg's law, the long period (L) was estimated using relationship $L \approx 2\pi/q_{max}$, where q_{max} is the (first order) maximum on the Iq^2 vs q curve. The one-dimensional (1D) correlation function of the electron density distribution, $K(z)$, was calculated from the measured (relative) scattering intensity $I(q)$ using eq 3:

$$K(z) = \frac{1}{r_e{}^2(2\pi)^3}\int_0^\infty \cos(qz)4\pi q^2 I(q)\, dq \quad (3)$$

where z is the distance.

D. Phase Composition and Molecular Mobility by Low-Field ^{1}H NMR T_1 and T_2 Relaxometry. Low-field ^{1}H NMR T_1 and T_2 relaxation experiments were performed on static samples at 26 °C on a Bruker Minispec mq-20 NMR spectrometer. This spectrometer operates at a proton resonance frequency of 20 MHz. The length of the 90° pulse, the dead time of the receiver, and the dwell times were 2.8, 7, and 0.5 μs. A BVT-3000 temperature controller was used for temperature regulation with an accuracy of ±0.1 °C. The decay of the transverse magnetization relaxation (T_2 decay) was measured with the solid-echo (SEPS) and Hahn-echo (HEPS) pulse sequences.[61] The SEPS and the HEPS decays were combined in one file and the file was fitted with a linear combination of the Abragamian,[62] Gaussian, and exponential functions:

$$A(t) = A(0)^s \exp[-(t/2T_2{}^s)^2][\sin(at)/at] + A(0)^i \exp[-(t/T_2{}^i)^2] + A(0)^l \exp[-(t/T_2{}^l)] \quad (4)$$

Here short, intermediate, and long relaxation times, $T_2{}^s$, $T_2{}^i$, and $T_2{}^l$, respectively, were assigned to the relaxation of the rigid fraction, which mainly originate from crystalline phases and small amounts of rigid noncrystalline fraction $T_2{}^s$, largely immobilized (constrained) amorphous fraction $T_2{}^i$, and mobile amorphous fraction $T_2{}^l$. The fraction of the relaxation components, as designated in the text by % $T_2{}^{index} = \{A(0)^{index}/[A(0)^s + A(0)^i + A(0)^l]\} \times 100\%$, represents the weight fraction of these phases.

The longitudinal magnetization relaxation (T_1 relaxation time) was measured using the inversion−recovery pulse sequence with the solid-echo detection of the signal amplitude: $180°_x - t_{inv} - 90°_x - t_{se} - 90°_y - t_{se} -$ [acquisition of the amplitude of the solid-echo maximum $A(0)^{inv}$ as a

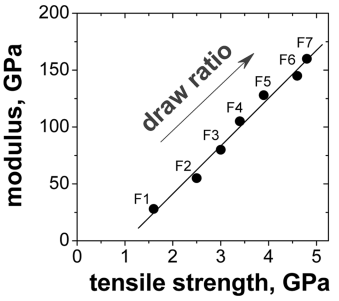

Figure 2. Relationship between the modulus and the tensile strength of gel-spun UHMWPE fibers. The line is meant as a guide to the eyes.

function of t_{inv}]. The dependence of $A(t_{inv})$ on t_{inv} was fitted using a two-exponential function:

$$A(t_{inv}) = A^a(0)[1 - 2\exp(-t_{inv}/T_1^a)] + A^b(0)[1 - 2\exp(-t_{inv}/T_1^b)] \quad (5)$$

It should be noted that the biexponential T_1 relaxation could be due to micro/macroscopic heterogeneity of fibers, as described in the literature,[11−14] and a slow spin-diffusion process between the rigid and mobile domains, as will be discussed below. The average T_1 relaxation time (T_1^{av}) was determined as follows:

$$1/T_1^{av} = f^a/T_1^a + (1 - f^a)/T_1^b \quad (6)$$

where $f^a = A^a(0)/[A^a(0) + A^b(0)]$. The recycle delay time for all experiments was then $5T_1^b$, where $T_1^b \gg T_1^a$.

More information is provided in the Supporting Information.

E. ^{1}H NMR Spin-Diffusion Experiments and Data Analysis. High-field ^{1}H NMR spin-diffusion experiments were performed at room temperature on a Bruker AV700 NMR solid-state spectrometer at a proton frequency of 700.2 MHz. ^{1}H NMR data were recorded for nonspinning samples that were placed in a 3.2 mm cross-polarization magic-angle spinning (CPMAS) probe. The dead time of the spectrometer, the duration of the 90° pulse, the dwell time, and the recycle delay time were 2.5 μs, 1.9 μs, 2 μs, and 3 s, respectively. ^{1}H spin-diffusion measurements were performed using the general setup consisting of the DQ dipolar filter, a spin-diffusion period, and an acquisition period.[63−65] The pulse sequence was: $[(\pi/2)_{x+\phi}-\tau-(\pi/2)_{-x+\phi}]$−DQ evolution−$[(\pi/2)_y-\tau-(\pi/2)_{-y}]-t-(\pi/2)_x$−acquisition, where the first block represents the DQ dipolar filter and t is the spin-diffusion time. The phases of the $\pi/2$ radio-frequency pulses in the first block of DQ coherence excitation had a phase cycle of four steps, i.e., $\phi = (0,1,2,3) \times (\pi/2)$ for selection of even-order coherences. More details on the experiment and data analysis are provided in the Supporting Information.

III. RESULTS

A. Mechanical Properties of Fibers. The term "draw ratio" is often used for describing the processing−structure−property relationships of fibers. However, the macroscopic draw ratio does not necessarily correspond to the drawing-induced chain extension because elastic chain contractions and slippage processes occur at different stages of fiber processing. The modulus and the tensile strength of UHMWPE fibers increases linearly with increasing draw ratio (Figure 2), and this is very often the case for gel-spun UHMWPE fibers. The modulus/tensile strength ratio itself depends on the type of process, the conditions therein, and especially the molecular weight, polydispersity, number, and the type of branching in UHMWPE used for the fiber spinning. At very high draw ratios, the modulus/tensile strength ratio often tends to increase due to the formation of local defects and chain scissions (which affects the tensile strength but has almost no effect on the modulus); however, this is not observed here.

Table 1. Mechanical Properties and Phase Composition (in wt %) of Gel-Spun UHMWPE Fibers[a]

			phase composition, wt %[b]		
fiber	tensile strength, GPa	modulus, GPa	orthorhombic crystals	monoclinic crystals	amorphous phase
F1	1.6	28	88.8	0.7	10.4
F2	2.5	55	90.2	1.8	8.0
F3	3.0	80	91.5	2.9	5.6
F4	3.4	105	92.2	3.2	4.6
F5	3.9	128	90.4	4.4	5.2
F6	4.6	145	91.8	3.6	4.6
F7	4.8	160	92.2	4.3	3.5

[a] The phase composition is determined by WAXS. [b] The average fitting error of WAXS profiles is 0.01 wt % for the orthorhombic phase, 0.08 wt % for the monoclinic phase, and 0.03 wt % for the amorphous phase (see the Supporting Information).

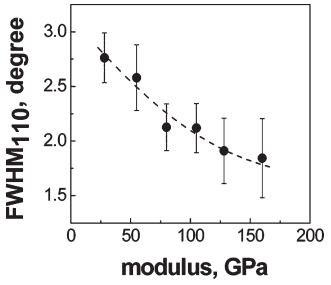

Figure 3. ($FWHM_{110}$) against the modulus of gel-spun UHMWPE fibers. Data points show the average value of ($FWHM_{110}$) measured at 10−12 different positions of a single filament. Error bars indicate the standard deviation σ, and the dashed line is meant as a guide to the eyes.

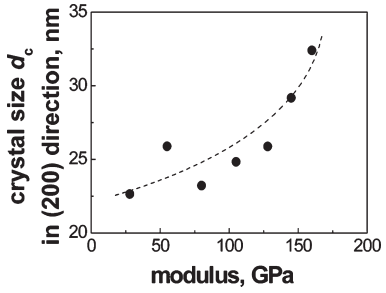

Figure 4. Average crystal size (d_c) in the (200) direction (perpendicular to the fiber axis) as a function of the modulus of gel-spun UHMWPE fibers. The dashed line is meant as a guide to the eyes.

B. WAXS Results. The phase composition (in wt %), as estimated by WAXS, is provided in Table 1. The chain orientation, as expressed by $FWHM_{110}$, is plotted against the modulus of fibers in Figure 3, which shows an increase in chain orientation with drawing. The Herman's orientation parameter $\langle P_2\rangle_{002}$ exceeds 0.998 for all fibers, indicating (1) a very high orientational order of crystals and (2) that the FWHM is more suitable than $\langle P_2\rangle_{002}$ for comparing the order parameter in this series of fibers.

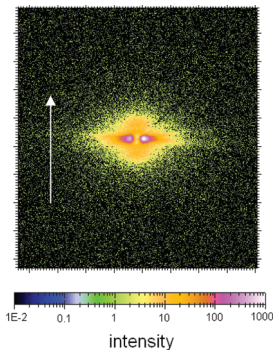

Figure 5. 2D SAXS pattern for gel-spun UHMWPE fiber with a modulus of 160 GPa. The measurements are performed on a bundle of pseudoparallel filaments with fiber axes indicated by the arrow on the pattern.

The size of orthorhombic crystals in direction perpendicular to the fiber axis (d_c), i.e., in the (200) direction, is plotted against fiber modulus in Figure 4. This size can be used as a measure of fibril diameter as was suggested for polyamide 6 fibers.[66]

C. SAXS Results. 2D SAXS patterns are shown for two fibers in Figures 1 and 5. These patterns are typical for fibers containing fibrils. The two spots on the pattern in the direction along the fiber axis are an indication of the long period of fibrils.[67] The streaks,[24] which are observed in the perpendicular direction, are due to scattering from the internal fibrillar morphology and a filament-to-air interface. The representative Iq^2 vs q curves along the fiber direction are shown in Figure 6. For the fiber with the modulus of 28 GPa, the second-order peak of the long period structures is still visible, whereas for fibers with higher moduli this peak disappears. This means that fibrils become more disordered along the fiber axis. The estimated long period is given in Table 2.

For semicrystalline polymers with lamellar crystallites, the long period as well as the lamellae thickness can be determined from the 1D correlation function of the electron density distribution, $K(z)$, using eq 3.[60] Fibrils in a semicrystalline fiber can be approximated by stacks of crystalline and amorphous blocks packed alternatively along the fiber axis.[24,66] Under this approximation, the size of fibrillar crystals along the fiber axis—the stem length (l_c) of the crystalline blocks—is estimated from the $K(z)$ function, as shown for two representative fibers in Figure 7. Since the fibers are highly crystalline even at low draw ratios, the smaller dimension in Figure 7 corresponds to thickness of the amorphous domains along the fiber direction (d_a). The shape of the $K(z)$ for the fibers with the modulus above 55 GPa is rather peculiar because the $K(z)$ function does not show a pronounced maximum at z values larger than that for the first minimum and even hardly exceeds zero at these z values. This might be caused by rather low signal-to-noise ratio at high q values due to high crystallinity. Therefore, the stem length of the crystalline blocks in fibrils cannot be determined for these fibers. It should be noted that fibrillar morphology in highly drawn UHMWPE fibers is very heterogeneous with a wide distribution of crystal size.[17,33] Therefore, the crystal stem length in fibrils corresponds to its volume average value.

G. Phase Composition and Molecular Mobility by Low-Field ^{1}H NMR Relaxometry. Low-field NMR relaxation experiments are used for determining the effect of draw ratio on phase composition and molecular mobility. ^{1}H T_1^{av} relaxation time allows us to compare the difference in fast (in the range of tens of MHz) local chain motions in the series of fibers. T_1^{av} increases from 0.61 to 1.75 s with increasing the modulus from 28 to 160 GPa. For largely immobilized materials, such as highly drawn fibers, this change corresponds to overall immobilization of polymer chains with increasing draw ratio. However, this experiment does not provide phase selective information due to the rather fast spin diffusion as will be discussed below. Therefore, ^{1}H T_2 relaxation experiments are used.

Figure 8 shows that the ^{1}H T_2 relaxation decay can be described with three components with a characteristic decay time (T_2), which is typical for the relaxation of rigid/crystalline materials (T_2^s), largely immobilized crystal−amorphous interface and constrained amorphous phase (T_2^i), and mobile amorphous materials with chain mobility comparable to that of rubbers (T_2^l).[68]

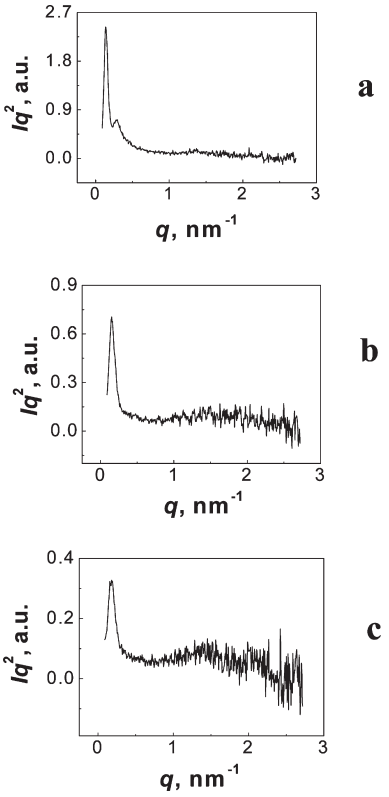

Figure 6. Dependence of Iq^2 on q for gel-spun UHMWPE fibers with the modulus of 28 GPa (a), 55 GPa (b), and 160 GPa (c). The dependence was measured in the direction along the fiber axis.

Table 2. Long Period (L) and Stem Length of Crystalline Blocks in Fibrils (l_c) As Determined by SAXS for Gel-Spun UHMWPE Fibers[a]

fiber modulus, GPa	L, nm	l_c, nm
28	45.2	37.3
55	41.5	n
80	38.9	n
105	36.9	n
128	35.8	n
145	35.3	n
160	35.0	n

[a] n: cannot be determined as described in the text.

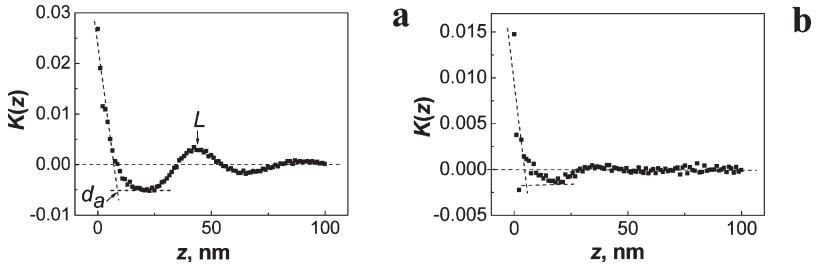

Figure 7. 1D electron density correlation function $K(z)$ for gel-spun UHMWPE fibers with the modulus of 28 GPa (a) and 80 GPa (b). The dashed lines are meant as a guide to the eyes. L and d_a correspond to the long period and the size of amorphous domains along the fiber direction in fibrils.

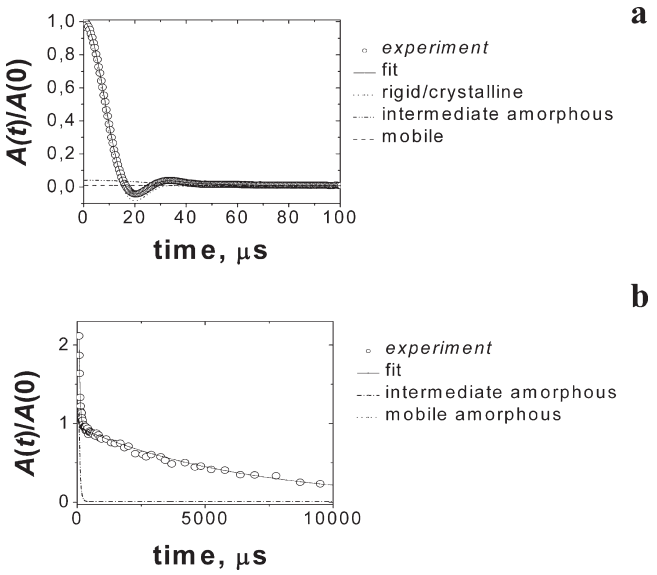

Figure 8. ^{1}H NMR T_2 relaxation decay for gel-spun UHMWPE fiber with the modulus of 105 GPa. The decay was measured at 26 °C using a combination of the solid-echo (a) and Hahn-echo pulse (b) sequences. The solid line represents the result of a least-squares adjustment of the decay (points) with a linear combination of the Abragamian, Gaussian, and exponential functions. The dotted lines show the separate relaxation components that originate from fiber domains with different molecular mobility.

Longer T_2 corresponds to a higher frequency and/or larger amplitude of molecular motions. The presence of highly mobile chain fragments in highly drawn PE has been also shown by wide-line ^{1}H and ^{2}H NMR experiments.[16,69]

Fiber drawing causes the following changes in molecular mobility and in phase composition (Figures 9 and 10, respectively). With increasing drawing, the amount of the rigid fraction, which is composed of orthorhombic and monoclinic crystals and small amount of rigid crystal−amorphous interface,[20] increases from 89% to 96% at the expense of amorphous fraction with intermediate chain mobility. The amount of rigid fraction is close to the total crystallinity that is measured by WAXS (Table 1 and Figure 10). The amount of mobile amorphous fraction hardly changes with draw ratio and equals to 0.95 ± 0.1%. The molecular mobility in crystalline phases and constrained amorphous fraction slightly increases upon drawing as follows from small increase in T_2^s and T_2^i values. Chain mobility in mobile amorphous fraction, as defined by T_2^l value, decreases upon increasing fiber modulus from 28 to 80 GPa and then increases for fibers with the higher modulus.

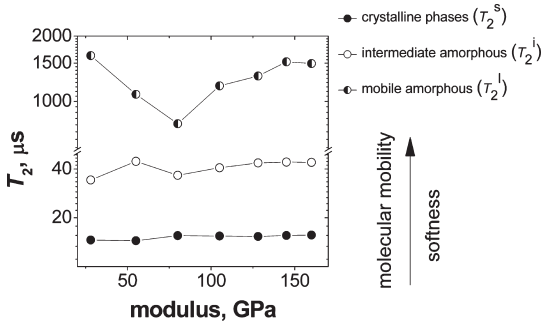

Figure 9. Changes in the molecular mobility in (1) the rigid fraction that is composed of orthorhombic and monoclinic crystals and a small amount of rigid crystal−amorphous interface, T_2^s relaxation; (2) constrained (intermediate) amorphous fraction, T_2^i relaxation; and (3) mobile amorphous fractions, T_2^l relaxation, of gel-spun UHMWPE fibers as a function of fiber modulus.

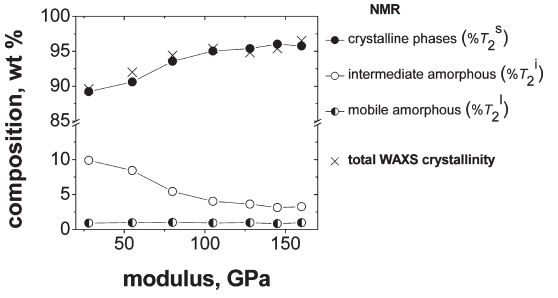

Figure 10. Changes in phase composition (in wt %) of gel-spun UHMWPE fibers with increasing fiber modulus. The phase composition is determined by $\%T_2^{index}$ values that are obtained by the analysis of ^{1}H NMR T_2 relaxation decay. The total WAXS crystallinity (composed of orthorhombic and monoclinic phases) is shown for comparison.

H. Domain Sizes by ^{1}H NMR Spin-Diffusion. The measurement of domain sizes by NMR spin-diffusion experiments requires the following four steps: (1) an optimization of a dipolar filter to obtain the highest selectivity to the different phases, (2) the knowledge of the spin-diffusion coefficients for modeling the experimental data, (3) the proper choice of a model which describes the morphology of the studied material, and (4) the appropriate solutions of the spin-diffusion equation for this specific morphology with the corresponding initial and boundary conditions.

The DQ dipolar filter is the most suitable one for the characterization of domain sizes in highly crystalline materials as discussed in the Supporting Information. Double-quantum coherences can

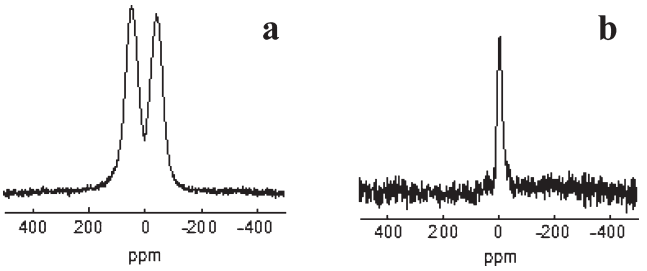

Figure 11. DQ-edited ^{1}H NMR spectra for a gel-spun UHMWPE fiber with the modulus of 160 GPa. The spectra were recorded using excitation and reconversion times of τ = 5 μs (a) and τ = 45 μs (b).

be generated by a pair of two radio-frequency pulses. For short excitation times (τ) mainly the DQ coherences of the methylene protons will be first generated. The optimum value of DQ filter time τ can be chosen by recording DQ buildup curves. The maximum of the DQ buildup curve for UHMWPE fibers appears at very short excitation/reconversion time τ of ~10−12 μs. The high selectivity of the DQ filter to physical phases in UHMWPE fibers is illustrated in Figure 11, which shows the DQ-edited NMR spectra recorded at short and long the excitation/reconversion time τ for a fiber with the modulus of 160 GPa. For short τ values, the DQ filtered ^{1}H NMR spectrum edits mainly the spin pairs with the strongest dipolar couplings in crystalline phases, whereas at longer τ values only the dipolar network from the amorphous fraction.

The values of the spin-diffusion coefficients D_R and D_M for rigid (mainly crystalline) and amorphous (mainly intermediate) phases can be determined by approximating the NMR line shapes obtained from standard wide-line ^{1}H NMR spectra of these fractions by Gaussian and Lorentzian functions, respectively. The spin-diffusion coefficients can be related to the second van Vleck moment of the NMR absorption lines which are, in turn, related to the full line width at half-height, $\Delta\nu_{1/2}$. The equations describing the spin-diffusion coefficients for crystalline (rigid) and amorphous (semirigid and mobile) phases are given by[70]

$$D_R = \frac{1}{12}\sqrt{\frac{\pi}{2\ln 2}}\langle r^2\rangle\Delta\nu_{1/2} \quad (7)$$

and

$$D_M = \frac{1}{6}\langle r^2\rangle[\alpha\Delta\nu_{1/2}]^{1/2} \quad (8)$$

where α is the cutoff parameter of the Lorentzian line and $\langle r^2\rangle$ is the mean-square distance between the nearest spins. An estimation of $\langle r^2\rangle \approx 0.0484$ nm^2 was reported for high-density polyethylene,[71] and we use this value for our computations. For UHMWPE fibers the values of D_R and D_M spin diffusivities evaluated from eqs 7 and 8 are given in Figure S1 of the Supporting Information.

The experimental data of ^{1}H spin-diffusion are shown in parts a and b of Figure 12 for the UHMWPE fibers with a modulus of 28 and 160 GPa, respectively. The time evolution of the integral intensities of the ^{1}H wide-lines corresponding to rigid and amorphous domains shows a decay and buildup behavior, respectively. The linear dependence in the initial diffusion time regime leads to the intercept $(t_0)^{1/2}$. The quasi-equilibrium states at the end of the diffusion process could be affected by the properties of the dipolar filter and the longitudinal relaxation time and therefore were not taken to define the intercept. From the $(t_0)^{1/2}$ intercept and the values of spin diffusivities and spin densities, the average thickness (d_R) of the rigid domain was evaluated in the approximation of the diffusion model discussed in the Appendix (eq A7) and shown in Figure 13.

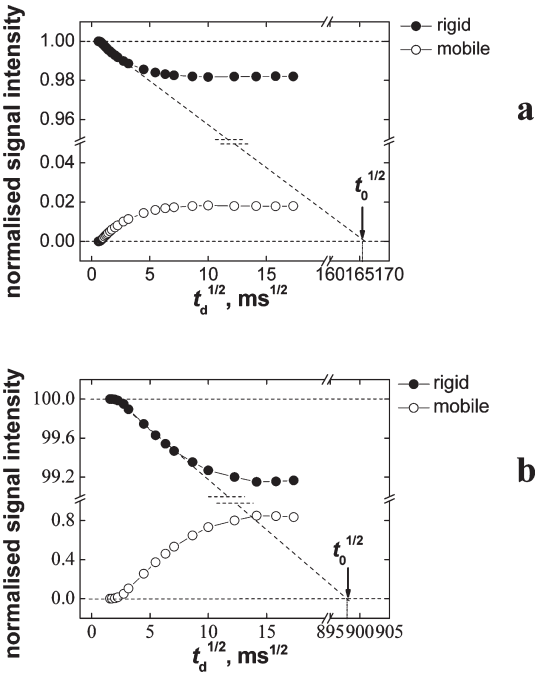

Figure 12. Spin-diffusion buildup and decay curves for crystalline (rigid) and amorphous domains in gel-spun UHMWPE fibers with the modulus of 28 GPa (a) and 160 GPa (b).

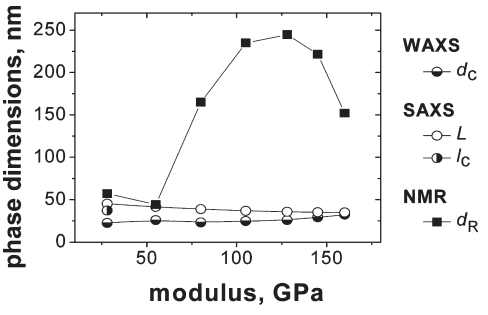

Figure 13. Average dimensions of crystalline/rigid domains against the modulus of gel-spun UHMWPE fibers. The mean size of rigid domains (d_R) is determined by an NMR spin-diffusion experiment. The long period (L), the stem length of the crystalline blocks in fibrils along the fiber axis (l_c), and the size of crystals in direction perpendicular to the fiber axis (d_c) as determined by SAXS and WAXS. It is noted that L and l_c values larger than ~70 nm cannot be determined by the conventional SAXS method.

IV. DISCUSSION

A. Phase Composition. All studied fibers are highly crystalline with orthorhombic phase providing the major contribution to crystallinity. The amount of orthorhombic and monoclinic phase increases by a few percent with increasing draw ratio (Table 1). Both WAXS and NMR methods show increase in the total crystallinity from ~89 to ~96 wt % with increasing fiber modulus

(Figure 10). The NMR T_2 relaxation method shows the presence of ~1 wt % of highly mobile chain fragments whose mobility is comparable to that of amorphous rubbers. This fraction can originate from chain fragments in nanovoids as suggested in a previous solid-state ^{1}H NMR study.[16] The presence of nanovoids in UHMWPE fibers was shown by a positron annihilation study[19] and by ^{129}Xe NMR.[20]

B. Molecular Mobility in Different Phases. The effect of fiber drawing on chain mobility in the crystalline and amorphous phases is provided by the T_2 relaxation experiment (Figure 9) and by wide-line NMR spectra recorded without and with the DQ filter.[20] Both NMR relaxometry and wide-line NMR spectroscopy are sensitive to changes in molecular mobility in the time window from approximately 10 to 1000 μs. Crystalline phases behave similar to a rigid sample with small amplitude motions of polymer chains in agreement with what was observed in wide-line ^{1}H NMR experiments on the same fibers.[20] Within the limits of experimental error, drawing hardly influences small-angle chain mobility in crystalline phases.[20] Proton T_2^r relaxation experiments have a lower selectivity to physical phases as compared to wide-line NMR spectra which are recorded using the DQ filter in the spin-diffusion experiment. The T_2^r relaxation time of the rigid fraction is mainly influenced by chain dynamics in the crystalline phases with a small contribution from crystal−amorphous interface. A small increase in T_2^r value was observed for fibers with the modulus above 80 GPa (Figure 9) that can be attributed to a small increase in chain dynamics at the interface and possibly in the crystalline phase due to an increasing amount of defects. Analysis of 2D WISE NMR spectra for the same fibers shows that drawing causes an increase in oscillation of methylene groups at the crystal−amorphous interface from ~8° to ~14°.[20] As far as the small amount of the mobile amorphous fraction is concerned, chain mobility decreases upon drawing for fibers with a modulus of up to 80 GPa and increases for fibers with higher modulus. An ESR study for another series of UHMWPE fibers also shows that for the draw ratios between 35 and 110 segmental mobility goes through a minimum.[72] These changes could be explained by an increase in chain elongation at lower draw ratios, causing a decrease in chain mobility. At higher draw ratios, some local disorder and voiding could cause an increase in chain mobility.

C. Dimensions of Crystals by SAXS, WAXS, and NMR. Different methods are used in the present study for determining dimensions of crystalline/rigid domains in UHMWPE fibers. The average crystal size in the direction perpendicular to the fiber axis (d_c) is determined by WAXS. The long period (L) and the stem length of crystalline blocks in fibrils (l_c) are obtained by SAXS. NMR spin-diffusion experiments are used to determine weight-average shortest-distance-across rigid domains, which are mainly formed by crystalline phases and largely immobilized chain fragments in either intra- and/or interfibrillar noncrystalline domains. These three methods provide a different contrast to semicrystalline morphology. WAXS and SAXS discriminate between crystalline and amorphous phases based on differences in electron density and its periodicity/variation at different length scales, with WAXS at the crystal lattice level and SAXS at larger length scale of semicrystalline superstructure level. NMR explores differences in chain mobility of different phases. The application of all three methods, which was not reported before for UHMWPE fibers, can provide a better understanding of fiber morphology.

Fiber drawing causes significant changes in phase dimensions as described here. The size of crystals in the direction perpendicular to the fiber axis increases from ~22 to ~33 nm with increasing draw ratio (Figure 4). The same trend has been previously observed for UHMWPE tape at later stages of drawing of a solution crystallized UHMWPE.[24] The SAXS peak intensity decreases continuously upon drawing (Figure 7), indicating a decrease in the concentration of fibrillar structures, similar to what is seen for drawing of solution-crystallized UHMWPE film.[24] The long period of fibrillar structures decreases by ~20% with an increasing draw ratio (Figure 13). Previous studies have shown that, at the later stages of drawing, the long period can either decrease with increasing draw ratio, as was observed for an extruded ultraoriented HDPE,[73] or remains constant, e.g. for a tape which was prepared by drawing of a solution-cast UHMWPE film.[24]

The NMR spin-diffusion method shows peculiar changes in average size of the rigid (mainly crystalline) domains (Figure 13). For the fiber with a modulus of 28 GPa, the average size of rigid domains is ~57 nm. This value does not largely deviate from the diameter and the stem length of crystalline blocks of fibrils as estimated by WAXS and SAXS, i.e., 22 and 37 nm, respectively. It should be mentioned that the NMR method measures weight-average smallest thickness of domains regardless of their orientation relative to the fiber axis. With an increasing draw ratio, the size of rigid domains, as measured by NMR, increases and then decreases for fibers with moduli larger than 128 GPa. The size of rigid domains largely exceeds dimensions of crystalline blocks in fibrils as determined by the X-ray methods (Figure 13).

The differences in domain sizes, as estimated using X-ray and NMR methods hints at the existence of large crystals, which are not detectable by conventional SAXS as was previously proposed for highly drawn solution-cast UHMWPE film.[24] It should be also mentioned that, if two adjacent crystals are separated by a rigid amorphous layer either intra- and/or interfibrillar, the NMR method will provide the total thickness of this rigid domain that is composed of crystalline and rigid amorphous phases. Therefore, the results might also suggest that drawing causes large immobilization of the amorphous layers separating adjacent crystals. However, the fraction of rigid amorphous material is small since the total crystallinity as determined by WAXS and the amount of rigid fraction is the same within experimental errors (Figure 10). Thus, the large differences in domain sizes as estimated using X-ray and NMR is explained by drawing-induced formation of large crystals that are invisible in the conventional SAXS experiment. NMR shows a decrease in the size of the rigid domains for fibers where the modulus is larger than 128 GPa. The long period of the fibrils in the fiber with a modulus of 160 GPa is even smaller than the stem length of crystalline blocks in fibrils of the fiber with a modulus of 28 GPa (Table 2). Thus, the SAXS method reveals fragmentation of fibrillar structures and NMR reveals the formation of large crystals structures at ultimate draw ratios.

D. Effect of Drawing on Fiber Morphology. Different types of morphological structures can be formed upon drawing of PE samples, i.e., shish-kebab and fibrillar morphologies, chain-extended crystals, and crystalline matrices with trapped defects. For a highly drawn solution-crystallized UHMWPE film, the morphology can be described as a mixture of fibrils and large, so-called chain-extended crystals.[24] The dimensions of the large crystals largely exceeds that of the crystals in fibrils. The term chain-extended crystals, which is often used in the literature, does not necessarily mean that crystals are formed by fully extended chains.[74] The possibility of the formation of crystals with fully

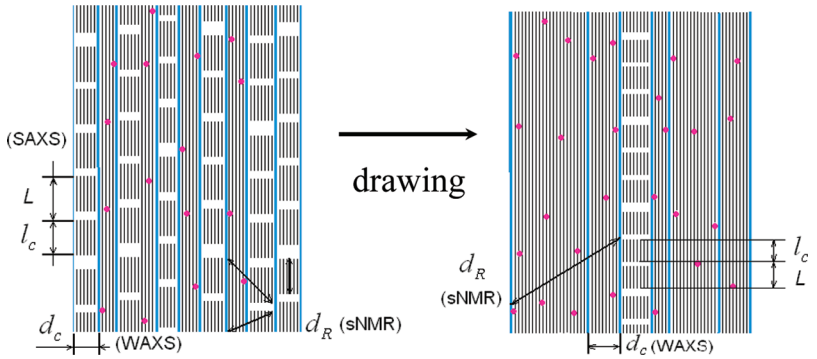

Figure 14. Schematic 2D drawing of the morphological features of gel-spun UHMWPE fibers with extreme draw ratios. The model shows the main morphological elements that are present in fibers with different draw ratios and not their dimensions. The thick lines show boundaries of the fibrils or large crystals with lost coherency across the lines. The large white areas correspond to amorphous domains and the small ones to voids and defects in large crystals. The designation of crystal dimensions, as measured by different method (Figure 13), is shown in this figure.

extended chains is very low due to residual chain entanglements that are trapped in the semicrystalline matrix during solvent removal in the gel-spinning used in the present study.

Results of X-ray and NMR methods suggest continuous transformation of fibrillar structures into large crystals at the late stage of fiber drawing. These large crystals do not show long-range periodicity even in a SAXS experiment (performed on JJ X-ray) with an upper detection limit of ~210 nm. One feature for such large crystals is that they do not show long period.[24] This can be caused either by (1) a large long period, which is beyond the detection limit of SAXS (above ~70 nm in the present study) or (2) an absence of regular periodicity of the crystalline−amorphous domains along the fiber axis. The large variations in crystal size dimensions were previously observed in drawn single-crystal UHMWPE mats.[33] Fiber drawing also causes an increase in the crystal size in the direction perpendicular to the fiber axis (Figure 4) due to a lateral merging of crystals of neighboring fibrils.[24] The transformation of fibrils into large crystals with randomly distributed defects can explain the crystallinity increase, which is observed by all methods used in the present study. Because of the high crystallinity of studied fibers, large crystals form the continuous crystalline matrix. The large crystals seem already to exist in fiber F1, and their fraction could be estimated by comparing volume crystallinity as measured by SAXS with weight crystallinity determined by WAXS. If fiber F1 would be composed of only fibrils, then volume crystallinity of 82.5% can be estimated from the ratio of l_c/L. Further assuming that the density of the crystalline and amorphous phases is not affected by drawing and equals 1.00 and 0.855 g/cm^3, respectively,[75] the weight crystallinity is estimated at 84.7 wt %. This value is lower than WAXS crystallinity for the same fiber, which is 89.5 wt %. From this difference, the volume fraction of large crystals in fiber F1 is estimated to be ~30%.

A peculiar result of this study is the decrease in the long period of remaining fibrillar structures (Table 2), which is accompanied by growth of large crystals. This decrease can be caused by (1) pulling out of some chains from amorphous phase into fibrillar crystals forming defects and/or (2) fragmentation of fibrillar crystals, which is initiated by defects which are trapped in crystals. The fragmentation of crystals can cause some local disordering with increasing draw ratios. As a result, the molecular mobility in the rigid fraction slightly increases as discussed above. Moreover, the higher order SAXS peak disappears, suggesting a decrease in the periodicity of crystalline−amorphous domains in the fibrils. The fragmentation can also explain the formation of nanovoids in UHMWPE fibers.[19,20]

Based on the results above, fiber morphology can be described in a relatively simple way by using a combination of two morphological models, i.e., the fibrillar morphology[22] and large crystals (crystalline matrix) with imbedded defects.[14,24] The suggested transformation of fiber morphology upon drawing is shown in Figure 14. The same morphological model was also suggested for explaining the mechanical properties of UHMWPE fibers using a fiber composite model.[76]

E. Effect of Drawing on Molecular Scale Phenomena. The drawing speed and temperature are two important parameters largely influencing the maximum achievable draw ratio of UHMWPE fibers.[8] Usually, a high draw ratio can be reached at a high drawing temperatures and low enough strain rates.[9] The temperature and the rate dependences of drawability strongly indicate that an activation process, which has been identified as the α_c-relaxation process (chain diffusion through crystals), is responsible for high drawability.[77] A sufficiently low entanglement density is another necessary condition for high drawability.[4−7] Commercial UHMWPE fibers are usually spun with a high winding speed from a semidilute solutions providing a good balance between fiber properties and productivities. For typical concentrations used, chains are not fully disentangled and not fully elongated in a spinneret. The remaining number of chain entanglements per a single chain can be estimated from M_w of UHMWPE and its concentration in the solution.[68,78,79] The number of residual chain entanglements is ~200 per chain in our case. During fast cooling of the solution and solvent removal, chain entanglements and conformational defects are trapped by fast growing crystals. The presence of the trapped entanglements and "frozen" defects in crystals cause a heterogeneous force distribution on the mesoscale that finally leads to a wide distribution of crystal sizes and shapes, distortions of the crystal lattice, a decrease of structural order, and a difference in local chain orientation.[17,80,81] Heterogeneous force distribution in loaded UHMWPE fibers was shown by Raman and WAXS studies.[27,41] One fraction of the C−C bonds exhibits high strain and the other one low strain.

Fiber drawing at elevated temperatures causes increase in crystallinity and "curing" of some of the conformational defects in crystals. However, drawing of fibers causes also an overall decrease in molecular mobility, as it follows from NMR T_1 relaxation data discussed above. The chain immobilization slows down the rate of the α_c-relaxation process,[77,82−84] which is important for structural

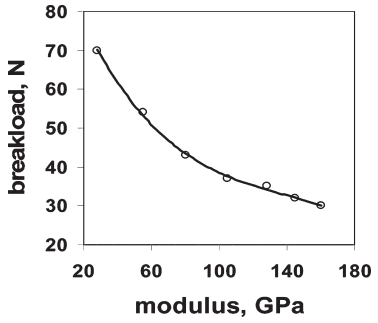

Figure 15. Tensile force at break of gel-spun UHMWPE fibers as a function of their modulus.

reorganizations required for the formation of "single" crystal-like structure of fibers. It was shown that the creep rate of drawn PE, which is largely influenced by the α_c-relaxation, decreases with increasing drawing.[85] Therefore, further fiber drawing causes accumulation of defects in crystalline regions, fragmentation of fibrillar structures, and the formation of nanovoids. These processes might be accountable for the significant drop in the tensile force at break of the fibers as a function of the modulus (Figure 15). This molecular picture is supported by the results of the present study.

F. Fiber Morphology and Mechanical Properties. Based on the above proposed model, there is a good correlation between the morphology development and the modulus of UHMWPE fibers at the final stage of drawing. Since the modulus is an intrinsic volume-average structural parameter of fibers, it is much less affected by the accumulation of defects in the crystalline regions, fragmentation of fibrillar structures, and the formation of nanovoids. This conclusion is also supported by the fact that the modulus of the studied UHMWPE fibers is not far from the calculated theoretical maximum modulus. As far as the tensile strength is concerned, this is more complex because this macroscopic parameter is significantly influenced by accumulation of defects as indicated by Smook[51] according to the Griffith theory.[52] The level of accumulation of defects depends on conditions that are used for fiber production. For samples prepared in a research laboratory, the amount of defects is smaller than for (semi)-commercially produced fibers used for the present study. This can be illustrated by the Griffith relation. This relation has provided the theoretical tensile strength for laboratory-scale prepared fibers of ~25 GPa.[51] The same relation for the (semi)commercial samples of this study provides the theoretical tensile strength of ~12 GPa. This value is close to the maximum tensile strength of (semi)commercial fibers reported so far.

Despite a significant increase in the tensile strength of fibers with increasing draw ratio (Figure 1), the tensile force at break decreases significantly at excessive drawing (Figure 15). The strength of fibers is closely related to the fraction of chains that carry the load. It should be mentioned that force distribution in loaded UHMWPE fibers is heterogeneous as shown by Raman and WAXS studies, and only a fraction of the C−C bonds carry the load.[27,41] The force that is required to break the fibers can thus be related to the absolute number of chains ruptures in the fracture surface. Previous studies of UHMWPE fibers have found an increase in the break load upon fiber drawing[86] or constant value of the break load that is independent of draw ratio.[53,87] This occurs despite the significant decrease in the fiber cross-sectional area due to an increase in crystallinity and orientation and because chains can slip through crystals and entanglement hooks, keeping constant the number of chains that carry the load. Chain slippages can be hindered due to a decrease in the rate of the α_c-relaxation process which can be caused by higher crystallinity, larger crystal size due to a higher entanglement density, and a high level of molecular inhomogeneity or to a too low drawing temperature. A decrease in the rate of chain slippages at further drawing will lead to breakage of the chains as the load on a single chain will become greater than the intrinsic breaking force of that chain.

The decrease in the tensile force at break, which is observed at excessive drawing (Figure 15), indicates that fiber structure is damaged during drawing. One of the most plausible explanations of this is chain scissions causing a reduction in molecular weight. This explains why the tensile strength at break is significantly lower than its theoretical maximum value for UHMWPE fibers. As far as the modulus is concerned, its value is rather close to the maximum theoretical value because of very high crystallinity and chain orientation of fibers as well as large crystal sizes.

V. CONCLUSIONS

The present study demonstrates that WAXS, SAXS, and ^{1}H solid-state NMR methods provide complementary information about the molecular-scale phenomena and changes in morphology that are caused by the drawing of gel-spun UHMWPE fibers. The following changes occur at the final stage of production of ultrastrong PE fibers. Crystallinity of fibers increases from ~89 to ~96 wt % with orthorhombic being the major crystalline phase. The amount of monoclinic phase increases upon drawing from ~1 to ~4.5 wt %. A small amount of a mobile amorphous fraction (~1 wt %) is present in all fibers. It is suggested that the origin of this fraction is caused by nanovoids in highly drawn UHMWPE fibers as shown by ^{129}Xe NMR.[20] Polymer drawing causes some disordering of the crystal structure. The orientation of crystals, which is already very high in partially drawn fibers, increases further with drawing. Drawing causes gradual transformation of fiber morphology from a fibrillar one to a morphology that is composed of fibrils and large, so-called, chain-extended crystals with trapped defects. The average crystal size in the direction perpendicular to the fiber axis (fibrillar crystals and chain extended ones) increases with drawing, whereas the size of fibrillar crystals along the fiber axis decreases.

Results of the present study suggest that the rate of the α_c-relaxation process relative to the strain rate during fiber drawing plays an important role in the development of fiber morphology toward perfect "single-crystal"-like structure. It appears that slowing down of the rate of the α_c-relaxation at the ultimate draw ratio causes fragmentation some of fibrils and local disordering of crystals. This accumulation of defects does not affect the development of fiber modulus as it is an intrinsic volume-average structural parameter. However, the development of the tensile strength will be affected in a significant way by the amount of defects whose level depends on the fiber processing conditions, i.e., laboratory versus (semi)commercial production.

■ APPENDIX

Theory of spin-diffusion in the initial rate approximation was used for determining the size of rigid domains. The following assumptions are made for an initial rate approximation of the spin-diffusion process. (i) The magnetization exchange is irreversibly taking place by a series of quasi-equilibrium states and,

therefore, could be described by a spin-diffusion equation. (ii) The solution of the spin-diffusion equation for a finite source and semi-infinite sink was used in this spin-diffusion regime.[70] It was assumed that spin-diffusion takes place in a heterogeneous matrix from a source R (rigid domains) with low segmental mobility into a semi-infinite sink M (mobile) with larger segmental mobility corresponding to the amorphous phase in semicrystalline polymers at temperatures above T_g. The above model is approximating the diffusion process for lamellar morphology of UHMWPE fibers only for short spin-diffusion time t, i.e., $t < d_R^2/D_R$, where d_R is the size of the rigid domains and D_R is the spin-diffusivity for the R domains. Furthermore, the interfacial region is incorporated into the rigid/crystalline and mobile amorphous fractions, as described in the Experimental Section. (iii) The general solution of the spin-diffusion equation for the composite medium of finite source and semi-infinite sink can be obtained using the solution for a one-dimensional (1D) composite medium. For a ε-dimensional diffusion process (ε = 1, 2, and 3 for 1D, 2D, and 3D), the solution of the spin-diffusion equation can be written simply as a product of the solutions for the 1D diffusion process. It is essential that the initial conditions must be expressible as a product of those for the single-variable problems taken separately.

Using the above assumptions the space and time evolution of the concentration of magnetization $m_R(\vec{r},t)$ in the R domains is given by[70]

$$m_R(\vec{r},t) = \frac{\rho_R\sqrt{D_R}m_{R0} + \rho_M\sqrt{D_M}m_{M0}}{\rho_R\sqrt{D_R} + \rho_M\sqrt{D_M}} - \frac{\rho_M\sqrt{D_M}(m_{M0} - m_{R0})}{\rho_R\sqrt{D_R} + \rho_M\sqrt{D_M}} \prod_{i=1}^{\varepsilon} \mathrm{erf}\left\{\frac{d_R/2 - x_i}{\sqrt{4D_R t}}\right\} \quad (A1)$$

where x_i are the coordinates of the vector $\vec{r}(x_1,x_2,x_3)$ and $x_i < d_R/2$. The error function is defined as

$$\mathrm{erf}(z) = \frac{2}{\sqrt{\pi}}\int_0^z e^{-x^2}\,dx \quad (A2)$$

A high efficiency dipolar filter is characterized by the initial concentration of magnetization: $m_{R0} \neq 0$ and $m_{M0} = 0$. For such conditions the eq A1 can be rewritten as

$$m_R(\vec{r},t) = \frac{\rho_R\sqrt{D_R}m_{R0}}{\rho_R\sqrt{D_R} + \rho_M\sqrt{D_M}} + \frac{\rho_M\sqrt{D_M}m_{R0}}{\rho_R\sqrt{D_R} + \rho_M\sqrt{D_M}} \prod_{i=1}^{\varepsilon} \mathrm{erf}\left\{\frac{d_R/2 - x_i}{\sqrt{4D_R t}}\right\} \quad (A3)$$

Using the above equations, we get for the time evolution of the integral intensity of the NMR signal from rigid domains R the following relationship:

$$\frac{I_R(t)}{I_0} = \frac{\rho_R\sqrt{D_R}}{\rho_R\sqrt{D_R} + \rho_M\sqrt{D_M}} + \frac{\rho_M\sqrt{D_M}}{\rho_R\sqrt{D_R} + \rho_M\sqrt{D_M}}\left\{1 - \frac{4\sqrt{D_R t}}{d_R}\left[\frac{1}{\sqrt{\pi}} - \mathrm{ierfc}\left(\frac{d_R}{4\sqrt{D_R t}}\right)\right]\right\}^{\varepsilon} \quad (A4)$$

where the integral error complement function is

$$\mathrm{ierfc}(z) = \int_z^{\infty}(1 - \mathrm{erf}(x))\,dx \quad (A5)$$

At the beginning of the spin-diffusion process, i.e., for short spin-diffusion times t, the quantity $d_R/(d_R t)^{1/2} \gg 1$ and $\mathrm{ierfc}(\infty) = 0$. It is evident from eq A4 that in the initial regime of the spin-diffusion process, i.e., for $t \ll {d_R}^2/D_R$, the time dependence of the NMR observable $I_R(t)/I_0$ is linear upon $\sqrt{t}$ and is given by

$$\frac{I_R(t)}{I_0} \approx \frac{\rho_R\sqrt{D_R}}{\rho_R\sqrt{D_R} + \rho_M\sqrt{D_M}} + \frac{\rho_M\sqrt{D_M}}{\rho_R\sqrt{D_R} + \rho_M\sqrt{D_M}}\left\{1 - \frac{4\varepsilon\sqrt{D_R t}}{\sqrt{\pi}d_R}\right\} \quad (A6)$$

The spin-diffusion decay curve (eq A6) is described by a straight line that intersects $\sqrt{t}$ axis at $(t_0)^{1/2}$. The domain thickness d_R for a ε-dimensional spin-diffusion process is determined from the equation

$$d_R \approx \frac{4\varepsilon}{\sqrt{\pi}}\frac{\rho_M\sqrt{D_R D_M}}{\rho_R\sqrt{D_R} + \rho_M\sqrt{D_M}}\sqrt{t_0} \quad (A7)$$

It should be noted that inaccuracy in the spin-density ratio and the values of spin-diffusivity could cause errors in the computed d_R values.

The quantity d_R can be evaluated also from the intercept of the initial straight line given by eq A6 to the horizontal line corresponding to the spin-diffusion data for quasi-equilibrium regime (see Figure 13). The intercept is denoted by $(t'_0)^{1/2}$ and its connection with the intercept $(t_0)^{1/2}$ can be easily evaluated from geometrical consideration

$$(t_0)^{1/2} = (t'_0)^{1/2}\left(1 - \frac{I_R^{qe}}{I_0}\right) \quad (A8)$$

where I_R^{qe}/I_0 is the ordinate of the spin-diffusion quasi-equilibrium data. The average thickness of the rigid domains can be evaluated also from the relationship

$$d_R \approx \frac{4\varepsilon}{\sqrt{\pi}}\frac{\rho_M\sqrt{D_R D_M}}{\rho_R\sqrt{D_R} + \rho_M\sqrt{D_M}}(t'_0)^{1/2}\left(1 - \frac{I_R^{qe}}{I_0}\right)^{-1} \quad (A9)$$

Equations A7 and A9 are equivalent, but the errors produced by using eq A9 also depend on I_R^{qe}/I_0. However, this approach provides NMR crystal dimensions lower that that of X-ray methods for fibers with low modulus. Because of the presence of large crystals in these fibers as discussed in section IV.C, the method is not justified.

■ ASSOCIATED CONTENT

Supporting Information. Experimental details. This material is available free of charge via the Internet at http://pubs.acs.org.

■ AUTHOR INFORMATION

Corresponding Author

*E-mail: victor.litvinov@dsm.com (V.M.L.); jianjun.xu@dsm.com (J.X.); demco@mc.rwth-aachen.de (D.E.D.).

■ ACKNOWLEDGMENT

The authors acknowledge the support from Deutsche Forschungsgemeinschaft (MO 682/12-1) and thank R. Marissen, R. J. Meier, S. N. Chavalun, H. van der Werff, T. Kidd, and T. Baughman for discussions and comments on the manuscript.

B. Stühn is appreciated for providing the program for calculation of the 1D electron density correlation function of the SAXS data. K. Joensen is appreciated for carrying out SAXS experiments for several fibers on JJ X-ray equipment which has a larger upper size detection limit.

REFERENCES

(1) Salem, D. R. *Structure Formation in Polymeric Fibers*; Salem, D. R., Ed.; Hanser Publishers: Munich, 2000.
(2) Rebouillat, S. In *High performance Fibers*; Hearle, J. W. S., Ed.; Woodhead Publishing Ltd.: Cambridge, UK, 2001; Chapter 2 and references therein.
(3) Young, R. J.; Lu, D.; Day, R. J.; Knoff, W. F.; Davis, H. A. *J. Mater. Sci.* **1992**, *27*, 5431.
(4) Lemstra, P. J.; Bastiaansen, C. W. M.; Peijs, T.; Jacobs, M. J. N. In *Solid Phase Processing of Polymers*; Ward, I. M., Coates, P. D., Dumoulin, M. M., Eds.; Hanser Publishers: Munich, 2000; p 172 and references therein.
(5) Smith, P.; Lemstra, P. J. *Makromol. Chem.* **1979**, *180*, 2983.
(6) Smith, P.; Lemstra, P. J.; Booij, H. C. *J. Polym. Sci., Polym. Phys. Ed.* **1982**, *20*, 2229.
(7) van Dingenen, J. L. J. In *High-Performance Fibers*; Hearle, J. W. S., Ed.; CRC Press: New York, 2001; p 62.
(8) Arridge, R. G. C.; Barham, P. J. *J. Polym. Sci., Polym. Phys.* **1978**, *16*, 1297.
(9) Kamamoto, T.; Tsuruta, A.; Tanaka, K.; Takeda, M.; Porter, R. S. *Macromolecules* **1988**, *21*, 470.
(10) Anandakumaran, K.; Roy, S. K.; Manley, R.; St., J. *Macromolecules* **1988**, *21*, 1746.
(11) Li, J.; Lee, Y.-W. *J. Mater. Sci.* **1993**, *28*, 6496.
(12) Wawkuschewski, A.; Cantow, H.-J.; Magonov, S. N.; Hewes, J. D.; Kocur, M. A. *Acta Polym.* **1995**, *46*, 168.
(13) Yeh, J.-T.; Lin, S.-C.; Tu, C. W.; Hsie, K.-H.; Chang, F.-C. *J. Mater. Sci.* **2008**, *43*, 4892.
(14) Berger, L.; Kausch, H. H.; Plummer, C. J. G. *Polymer* **2003**, *44*, 5877.
(15) Magonov, S. N.; Sheiko, S. S.; Deblieck, R. A. C.; Möller, M. *Macromolecules* **1993**, *26*, 1380.
(16) Hu, W.-G.; Schmidt-Rohr, K. *Polymer* **2000**, *41*, 2979.
(17) Grubb, D. T.; Prasad, K. *Macromolecules* **1992**, *25*, 4575.
(18) Chvalun, S. N.; Zubov, Yu.A.; Bakeev, N. F. *Polym. Sci.* **1993**, *35*, 285.
(19) Bamford, D.; Jones, M.; Latham, J.; Hughes, R. J.; Alam, M. A.; Stejny, J.; Dlubek, G. *Macromolecules* **2001**, *34*, 8156.
(20) Demco, D. E.; Melian, C.; Simmelink, J.; Litvinov, V. M.; Möller, M. *Macromol. Chem. Phys.* **2010**, *211*, 2613.
(21) Porter, R. S.; Wang, L. H. *J. Macromol. Sci., Rev. Macromol. Chem. Phys.* **1995**, *C35*, 63.
(22) Peterlin, A. *J. Polym. Sci.* **1965**, *C9*, 61.
(23) Gibson, A. G.; Davies, G. R.; Ward, I. M. *Polymer* **1978**, *19*, 683.
(24) van Aerle, N. A. J. M.; Braam, A. W. M. *J. Mater. Sci.* **1988**, *23*, 4429.
(25) Hofmann, D.; Schulz, E. *Polymer* **1989**, *30*, 1964.
(26) Barham, P. J.; Arridge, R. G. C. *J. Polym. Sci., Polym. Phys.* **1977**, *19*, 1177.
(27) Wong, W. F.; Young, R. J. *J. Mater. Sci.* **1994**, *29*, 520.
(28) Peterlin, A. *J. Mater. Sci.* **1971**, *6*, 490.
(29) Porter, R. S.; Wang, L.-H. *J. Macromol. Sci., Rev. Macromol. Chem. Phys.* **1995**, *C35*, 63.
(30) Ottani, S.; Ferracini, E.; Ferrero, A.; Malta, V.; Porter, R. S. *Macromolecules* **1996**, *29*, 3292.
(31) Takahashi, Y.; Ishida, T. *J. Polym. Sci., Part B: Polym. Phys.* **1988**, *26*, 2267.
(32) Uehara, H.; Kanamoto, T.; Kawaguchi, A.; Murakami, S. *Macromolecules* **1996**, *29*, 1540.
(33) Zubov, Y. A.; Chvalun, S. N.; Selikhova, V. I.; Konstantinopolskaya, M. B.; Bakeev, N. Ph. *Polym. Eng. Sci.* **1992**, *32*, 1316.
(34) Ania, F.; Baltá Calleja, F. J.; Bayer, R. K.; Tshmel, A.; Naumann, I.; Michler, G. H. *J. Mater. Sci.* **1996**, *31*, 4199.
(35) Tzou, D. I.; Schmidt-Rohr, K.; Spiess, H. W. *Polymer* **1994**, *35*, 4728.
(36) Matsuo, M.; Bin, Y.; Xu, C.; Ma, L.; Nakaoki, T.; Suzuki, T. *Polymer* **2003**, *44*, 4325.
(37) Alexander, L. E. *X-Ray Diffraction Methods in Polymer Science*; Wiley-Interscience: New York, 1969.
(38) Zhang, H.; Mo, Z. *Structure of Crystalline Polymers by X-ray Diffraction*; Chinese Science Publishing Group: Beijing, 2003; Chapter 9, pp 181−204.
(39) Murthy, N. S.; Barton, R., Jr. In *Industrial Applications of X-ray Diffraction*; Chung, H. F., Smith, K. D., Eds.; Marcel Dekker: New York, 2000; Chapter 19, pp 495−509.
(40) Crockford, C.; Geen, H.; Titman, J. J. *Solid State Nucl. Magn. Reson.* **2002**, *22*, 298.
(41) Moonen, J. A. H. M.; Roovers, W. A. C.; Meier, R. J.; Kip, B. J. *J. Polym. Sci., Part B: Polym. Phys.* **1992**, *30*, 361.
(42) Wang, D.; Klaassen, A. A. K.; Janssen, G. E.; De Boer, E.; Meier, R. J. *Polymer* **1995**, *36*, 4193.
(43) Hoogsteen, W.; Kormelink, H.; Eshuis, G.; Brinke, G.; Pennings, A. J. *J. Mater. Sci.* **1988**, *23*, 3467.
(44) Porter, R. S.; Kanamoto, T.; Zachariades, A. E. *Polymer* **1994**, *35*, 4979 and references therein.
(45) Mark, H. F. *Polymer Science and Materials*; Tobolsky, A. V., Mark, H. F., Eds.; Wiley Interscience: New York, 1971; p 236.
(46) Termonia, Y.; Meakin, P.; Smith, P. *Macromolecules* **1986**, *19*, 154.
(47) Penning, J. P.; van der Werff, H.; Roukema, M.; Pennings, A. J. *Polym. Bull* **1990**, *23*, 347.
(48) Hageman, J. C. L.; de Wijs, G. A.; de Groot, R. A.; Meijer, R. J. *Macromolecules* **2000**, *33*, 9098.
(49) Meier, R. J. *Macromolecules* **1993**, *26*, 4376.
(50) Hageman, J. C. L.; Meier, R. J.; Heinemann, M.; de Groot, R. A. *Macromolecules* **1997**, *30*, 5953.
(51) Smook, J. PhD Thesis, RU Groningen, The Netherlands, 1984.
(52) Griffith, A. A. *Philos. Trans. R. Soc. London, Ser. A* **1921**, *221*, 163.
(53) Ohta, Y.; Murase, H.; Hashimoto, T. *J. Polym. Sci., Part B: Polym. Phys.* **2005**, *43*, 2639.
(54) Marissen, R.; Simmelink, J. A. P. M.; Litvinov, V. WO 2008/131925 A1.
(55) Wilchinsky, Z. W. *J. Appl. Phys.* **1960**, *31*, 1969.
(56) Ohta, Y.; Kaji, A.; Sugiyama, H.; Yasuda, H. *J. Appl. Polym. Sci.* **2001**, *81*, 312.
(57) Lafrance, C.-P.; Pézolet, M. J.; Prud'homme, R. E. *Macromolecules* **1991**, *24*, 4948.
(58) Zhang, F.; Stühn, B. *Colloid Polym. Sci.* **2006**, *284*, 823.
(59) Hammersley, A. P. ESRF Internal Report ESRF97HA02T. "FIT2D: An Introduction and Overview"; Grenoble, 1997.
(60) Strobl, G. *The Physics of Polymers*, 2nd ed.; Springer: Berlin, 1996; Chapter 4, pp 150−153.
(61) Litvinov, V. M.; Penning, J. P. *Macromol. Chem. Phys.* **2004**, *205*, 1721.
(62) Abragam, A. *The Principles of Nuclear Magnetism*; Clarendon Press: Oxford, 1961.
(63) Buda, A.; Demco, D. E.; Bertmer, M.; Blümich, B.; Litvinov, V. M.; Penning, J.-P. *J. Phys. Chem. B* **2003**, *107*, 5357.
(64) Buda, A.; Demco, D. E.; Bertmer, M.; Blümich, B.; Litvinov, V. M.; Penning, J.-P. *Chem. Phys. Chem.* **2004**, *5*, 876.
(65) Baias, M.; Demco, D. E.; Istrate, D.; Popescu, C.; Blümich, B.; Möller, M. *J. Phys. Chem. B* **2009**, *113*, 12136.
(66) Huisman, R.; Heuvel, H. M. *J. Polym. Sci., Polym. Phys.* **1976**, *14*, 941.
(67) Chuah, H. H.; Porter, R. S. *J. Polym. Sci.* **1984**, *22*, 1353.
(68) Litvinov, V. M. *Macromolecules* **2006**, *39*, 8727.
(69) Deckmann, H.; Möller, M.; Govaert, L.; Lemstra, P. J. In *Integration of Polymer Science and Technology*, Part 5; Elsevier Appl. Sci. Publ.: Amsterdam, 1991; pp 276−290.

(70) Demco, D. E.; Johansson, A.; Tegenfeldt, J. *Solid State Nucl. Magn. Reson.* **1995**, *4*, 13.
(71) Hedesiu, C.; Demco, D. E.; Kleppinger, R.; Adams Buda, A.; Blümich, B.; Remerie, K.; Litvinov, V. M. *Polymer* **2007**, *48*, 763.
(72) Tiňo, J.; Klimová, M.; Chodák, I. *Polym. Int.* **1996**, *39*, 231.
(73) Zachariades, A. E.; Mead, W. T.; Porter, R. S. *Chem. Rev.* **1980**, *80*, 351.
(74) Bassett, D. C. *Polymer* **1976**, *17*, 460.
(75) Brandrup, J., Immergut, E. H., Eds.; *Polymer Handbook*, 2nd ed.; John Wiley & Sons: New York, 1975; p V-15.
(76) Clements, J.; Jakeways, R.; Ward, I. M. *Polymer* **1978**, *19*, 639.
(77) Hu, W.-G.; Schmidt-Rohr, K. *Acta Polym.* **1999**, *50*, 271.
(78) Fetters, L. J.; Lohse, D. J.; Richter, D.; Witten, T. A.; Zirkelt, A. *Macromolecules* **1994**, *27*, 6439.
(79) Ramos, J.; Vega, J. F.; Theodorou, D. N.; Martinez-Salazar, J. *Macromolecules* **2008**, *41*, 2959.
(80) Hu, X.-P.; Hsieh, Y.-L. *Polym. J.* **1998**, *30*, 771.
(81) Riekel, C.; Cedola, A.; Heidelbach, F.; Wagner, K. *Macromolecules* **1997**, *30*, 1033.
(82) Yao, Y.-F.; Graf, R.; Spiess, H. W.; Lippits, D. R.; Rastogi, S. *Phys. Rev. E* **2007**, *76*, 060801 (R).
(83) Yao, Y.; Chen, Q. *Annu. Rep. NMR Spectrosc.* **2010**, *69*, 199.
(84) O'Connell, P. A.; Bonner, M. J.; Duckett, R. A.; Ward, I. M. *J. Appl. Polym. Sci.* **2003**, *89*, 1663.
(85) Ward, I. M.; Wilding, M. A. *J. Polym. Sci., Polym. Phys. Ed.* **1984**, *22*, 561.
(86) Wang, J.; Smith, K. J., Jr. *Polymer* **1999**, *40*, 7261.
(87) Pennings, J. P.; Dijkstra, D. J.; Pennings, A. J. *J. Mater. Sci.* **1991**, *26*, 4721.
(88) Clauss, J.; Schmidt-Rohr, K.; Spiess, H. W. *Acta Polym.* **1993**, *40*, 1.
(89) VanderHart, D. L.; McFadden, G. B. *Solid State Nucl. Magn. Reson.* **1996**, *7*, 45.